applied sciences

MDPI

Article

All-t_{2g} Electronic Orbital Reconstruction of Monoclinic MoO_2 Battery Material

Luis Craco [1,2,*] and Stefano Leoni [3,*]

1 Instituto de Física, Universidade Federal de Mato Grosso, Cuiabá 78060-900, MT, Brazil
2 Leibniz Institute for Solid State and Materials Research Dresden, Helmholtzstr. 20, D-01069 Dresden, Germany
3 School of Chemistry, Cardiff University, Cardiff CF10 3AT, UK
* Correspondence: lcraco@fisica.ufmt.br (L.C.); leonis@cardiff.ac.uk (S.L.)

Received: 2 July 2020; Accepted: 15 August 2020; Published: 19 August 2020

Featured Application: The dielectric function and optical conductivity are used to evaluate voltage-capacity profiles, as their shape is rooted in the multi-orbital nature of the redox process in battery materials. This represents a firm approach to characterise materials for energy storage, and battery materials in particular, and offers a robust predictive framework for novel battery materials, one that can be rapidly matched to measurable quantities.

Abstract: Motivated by experiments, we undertake an investigation of electronic structure reconstruction and its link to electrodynamic responses of monoclinic MoO_2. Using a combination of LDA band structure with DMFT for the subspace defined by the physically most relevant Mo 4*d*-bands, we unearth the importance of multi-orbital electron interactions to MoO_2 parent compound. Supported by a microscopic description of quantum capacity we identify the implications of many-particle orbital reconstruction to understanding and evaluating voltage-capacity profiles intrinsic to MoO_2 battery material. Therein, we underline the importance of the dielectric function and optical conductivity in the characterisation of existing and candidate battery materials.

Keywords: correlated materials; battery materials; DMFT

1. Introduction

Understanding correlated materials remains a problem of enduring interest in condensed matter physics. So far, lot of attention has been focused on the way a material evolves from a metallic to an insulating state [1]. Electron–electron and electron–lattice interactions are well known driving forces behind metal-to-insulator instabilities. In a Peierls system a metal becomes an insulator via lattice distortion, which usually doubles the crystal unit cell. This in turn opens a bonding-antibonding band gap at the Fermi level (E_F), whereby the lowering of the one-particle bonding state compensates the energy cost incurred by the lattice distortion [2]. This situation is similar to a one-dimensional spin-Peierls effect [3], in which a reduction of magnetic energy of spins on dimers also induces lattice distortions. Hence, both the electronic- and the spin-Peierls instabilies are triggered by the coupling to the vibrational excitations of the crystal, i.e., the phonons. On the other hand, the Mott–Hubbard metal-insulator transition is caused by strong Coulomb correlations that prevent double occupancy of electrons with opposite spins on the same electronic state [1]. However, in materials like VO_2 both scenarios seem to be cooperative [2]. As a result, concomitant quantum phase transitions involving lattice and electronic degrees of freedom become possible. The observed first-order transition occurring around $T = 340$ K [4] in VO_2 is dubbed Mott–Peierls, because the lattice distortion is assisted [5] by the presence of correlated electronic states in close proximity to Mottness [6]. In this regime,

dynamical scatterings arising from multi-orbital (MO) electron–electron interactions should be taken into consideration to understand the physical properties intrinsic to materials showing exotic phase transitions upon external perturbations. In this work we show that a reconstructed orbital state induced by MO electronic interactions [7] also holds true for MoO_2. We shall notice here, however, that not only at the interfaces of oxide heterostructures [7] but also in bulk materials, both the modification of the nearby surroundings and intrinsic dynamical electron–electron interactions can significantly affect the electronic structure of *d*-band materials, in particular the occupation and energy position of the *d*-shell levels. These and related nontrivial effects are fingerprints of electronic orbital reconstruction. Within a correlated multi-band framework [8], the active *d*-orbitals are normally reconstructed relative to their bare, band values. This behavior brings to the fore the most fundamental aspect in correlated electronic structure calculations, i.e., how the reconstructed orbitals in quantum materials are dynamically reshaped by realistic multi-orbital electron–electron interaction effects.

Interest in molybdenum oxides is particularly motivated by their application in a wide variety of fields such as flexible electronics [9], solid fuel cells [10], gas sensors, catalysis, diffusion barrier [11], and storage lithium ion batteries [12–16]. Importantly, MoO_2 is considered to be one of the most studied anode systems for lithium ion batteries [13,16]. Both for fundamental science [17] and for applications, MoO_2 is relevant in view of the quantum nature of its metallic conductivity [9,18] and the possible reduced localization of 4*d* electrons as compared, for example, to 3*d* electrons of VO_2 [19]. MoO_2 is isostructural with VO_2 at room temperature. Similar to what is found for the d_{xy} orbital of VO_2 [5], electronic structure calculations within the monoclinic phase show large bonding-antibonding splitting of the $d_{x^2-y^2}$ band in MoO_2 [19,20]. This behavior is consistent with metal-metal dimerization parallel to the *c*-axis [21]. Moreover, band structure calculations [20] suggest that the monoclinic structure results from an embedded Peierls-like instability, which mediates the metal-metal overlap along chains parallel to the rutile *c*-axis embedded in a background of the dispersing xz, yz states. This scenario has been used to analyze Fermi surface topology and band dispersion of MoO_2 probed, respectively, in de Haas-van Alphen and angle-resolved photoemission spectroscopy (ARPES) experiments [19].

A closer inspection of experiments reveals several exotic properties in MoO_2 which are fundamentally different from simple metals, implying that many-particle correlation effects beyond the local density approximation (LDA) need to be considered. Experimental observations supporting this view are: ARPES [19] and angle-integrated PES [20] measurements show signatures of pseudogap like low-energy features close to the Fermi energy, implying substantial correlation effects. An optical conductivity study reveal a Drude part at low energies followed by a broad bump around 0.8 eV and high-energy features centered above 4 eV [22]. Noteworthy, the first bump was taken as an evidence that normal metallic conduction is not occurring in MoO_2. Noticeable carrier mass enhancement $m^\star/m \approx 5$, a value close to that found for VO_2 [4], reinforces the relevance of dynamical electronic interactions. Finally, resistivity data of Ref. [11] display Fermi liquid (FL) behavior ($\rho(T) = \rho_0 + AT^2$), however, in several other cases it deviates significantly [13,18,23] from this canonical T^2-dependence of good FL metals. In fact, MoO_2 appears to be a poor-metal at low-T, with a sample dependent resistivity upturn below $T^\star \approx 100$ K [13,23], implying substantial correlation effects in the Mo 4*d*-subshell crossing E_F. How might scattering processes involving charge and orbital fluctuations produce the observed correlated metal? How robust is the bare bonding-antibonding splitting against sizable electron–electron interactions? Which are the electronic fingerprints of a reconstructed orbital bonding-antibonding state [5] in monoclinic MoO_2?

In this work we address these questions by modeling the correlated electronic structure of monoclinic MoO_2 on the basis of LDA band structure calculations combined with dynamical mean-field theory (DMFT) [8]. Likewise for VO_2, we clearly find an orbital-selective (OS) metallic behavior which results from sizable MO electron–electron interactions in the Mo 4*d* subshell near E_F. Our results are important for understanding the competition between itinerancy and local, MO Hubbard interactions in MoO_2. In particular, low-energy pseudogap-like features probed in photoemission experiments are shown to be driven by a correlation-assisted orbital reconstruction, reflecting incoherent charge

localization due to the formation of dynamical metal-metal ion bonds. Our scenario suggests the essential role played by (local) MO Coulomb repulsion acting as the emerging dynamical interaction for the many-fold metal-pair reconstruction in materials with monoclinic distortions.

To date, the relevance of local correlations on the electronic structure has been studied within density-functional-theory plus U (DFT+U), for example in molybdenum oxides [24] or other anodic dichalcogenide battery materials like MoS_2 [25]. While DFT+U calculations yield the correct spin and orbital orders, by construction this is a ground state theory and therefore cannot describe dynamical many-particle effects. Here, we extend ab initio density-functional calculations to incorporate these effects within the LDA+DMFT method [8]. Interestingly, this method has been applied to elucidate the electronic structure of $SrMoO_3$ [26], supporting the hypothesis of multi-orbital dynamical interactions in Mo-base materials in general. Focussing on monoclinic MoO_2, we study its one- and two-particle responses, providing a many-particle description of PES, optical conductivity and gavanolstatic data relevant to MoO_2 battery material [16,27].

To reveal the orbital-selective metallic phase probed in spectroscopy and electric transport experiments, as well as the coexistence of pseudogaped and normal metallic states, in this work we employ the density functional theory plus dynamical mean-field theory (DFT+DMFT) scheme [8], which by construction takes into consideration the most relevant all-electron degrees of freedom and intra- and inter-orbital correlation effects in the solid. The DFT+DMFT scheme is an ideal and realistic starting point towards understanding Mott metal-to-insulator transitions, the nature of Fermi and non-Fermi liquid metallic states and, on more general grounds, the role played by dynamical electronic correlations in multi-orbital systems. DFT+DMFT provides cogent answers to fundamental questions, including why orbital, magnetic and superconducting (conventional or not) orders in correlated electron and topological quantum systems set in at zero and finite temperatures, and how they might change upon application of external perturbations (pressure, chemical doping, magnetic and electric fields, etc.). Within our single site DFT+DMFT scheme, dimer-dimer correlations are treated on LDA level. Extensions of the single-site DMFT scheme to explicitly includes inter-site interactions, based, for example, on cluster DMFT approaches, may be considered to describe dynamical dimer-dimer correlations in MoO_2 and related materials. Nonetheless, the good agreement between the frequency dependence of the self-energy (imaginary and real parts) we have recently derived for baddeleyite-type NbO_2 [28] and that of the distorted, body-centered tetragonal (bct) NbO_2 crystal obtained using cluster DFT+DMFT calculations[29], fully qualifies single-site DFT+DMFT approximation for the study of the electrodynamic behaviour of MoO_2 battery material. Here, one-particle LDA density-of-states are computed using the non-fully relativistic version of the PY-LMTO code [30]. To incorporate the effects of dynamical electronic correlations within the t_{2g} orbital sector of MoO_2 bulk crystal, we used the multi-orbital iterated-perturbation-theory (MO-IPT) as an impurity solver of the many-particle problem in DMFT, as described in detail in Refs. [31,32]. The state-of-the-art DFT+DMFT(MO-IPT) implementation used here correctly describes disorder, pressure, electric and magnetic fields, spin-orbit, and temperature effects in multi-band electronic systems. The computation of optical conductivity was carried out using the $d = \infty$ (DMFT) approximation [33–35].

2. Results and Discussion

Earlier band structure calculations [20] for monoclinic MoO_2 have shown that the most relevant electronic subshell near E_F in this compound originates from Mo $(4d)$ t_{2g}-orbitals. Here, the t_{2g} bands of MoO_2 [19] were obtained using the linear-muffin-tin orbital (LMTO) scheme [30]. Within LDA, the one-electron part for MoO_2 is $H_0 = \sum_{\mathbf{k},a,\sigma} \epsilon_a(\mathbf{k}) c^\dagger_{\mathbf{k},a,\sigma} c_{\mathbf{k},a,\sigma}$, where $a = (x^2 - y^2, yz, xz)$ label (in Moosburger-Will's notation [19]) the diagonalized $4d$ bands close to E_F, see Figure 1. These three diagonalized orbitals are the relevant one-particle inputs for MO-DMFT which generates an orbital-selective bad-metallic state for $U \geq 4.0$ eV as shown below. The correlated many-body Hamiltonian for MoO_2 reads $H_{int} = U \sum_{i,a} n_{ia\uparrow} n_{ia\downarrow} + \sum_{i,a\neq b} [U' n_{ia} n_{ib} - J_H \mathbf{S}_{ia} \cdot \mathbf{S}_{ib}]$. Here, $U' \equiv U - 2J_H$ with U (U') being the intra- (inter-) orbital Coulomb repulsion and J_H is the Hund's rule

coupling. The DMFT self-energy, $\Sigma_a(\omega)$, requires a solution of the MO quantum impurity model self-consistently embedded in an effective medium. [8] We use the MO iterated perturbation theory (MO-IPT) as an impurity solver for DMFT. [31] This perturbative, many-body scheme has a proven record of describing dynamical effects of correlated electron systems.

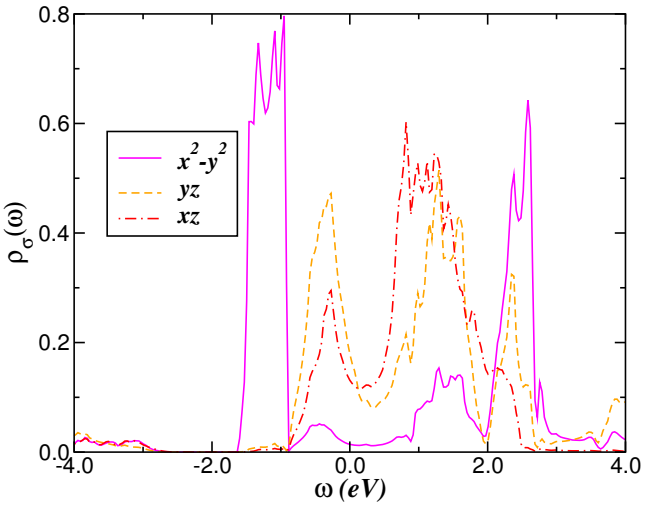

Figure 1. Partial LDA densities-of-states (DOS) of MoO_2 within the monoclinic symmetry. Notice the splitting of LDA the bands into bonding and antibonding branches in the projected $d_{x^2-y^2}$ DOS, a characteristic property of monoclinic materials.

2.1. Correlated Electronic Structure

We now present our results. We start with the monoclinic (space group $P2_1/c$) structure of MoO_2 (Figure 2) with lattice constants and monoclinic angle as in Refs. [24,36]. In agreement with previous studies [19,20], one-electron band structure results for the LDA spectral function (Figure 1) shows partially occupied 4*d* orbitals with pronounced bonding-antibonding splitting in the $x^2 - y^2$-orbital due to dimerized metal-pairs in the monoclinic crystal structure. In what follows, we employ the LDA+DMFT scheme [8] to treat local MO interactions present in MoO_2 and related transition metal dioxides. Consistent with experimental observations [13,19,20,22], we show that the metallic phase of MoO_2 is correlated with appreciable changes in the electronic structure compared to LDA.

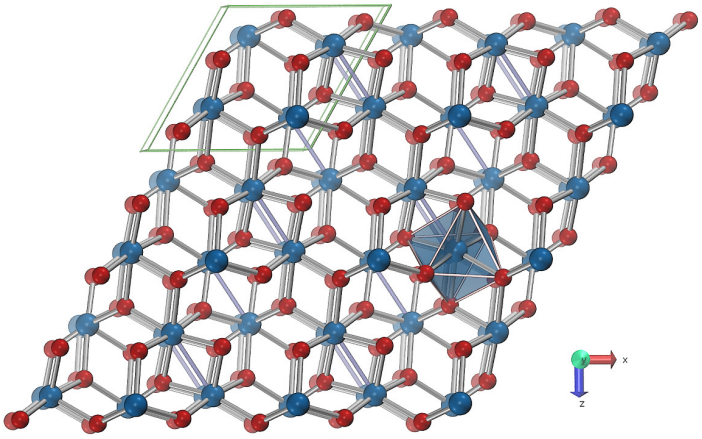

Figure 2. Crystal structure of MoO_2 of monoclinic symmetry (Mo blue, O red), atomic coordinates and cell parameters are taken from Ref. [36]. Short Mo-Mo contacts are represented as blue sticks. The monoclinic unit cell is highlighted in green. The distorted octahedral coordination of Mo by O is represented as transparent polyhedron. A $3 \times 2 \times 3$ supercell was chosen.

In Figures 3 and 4 we display our LDA+DMFT results for different values of U and fixed $J_H = 0.7$ eV. These results show how MO electron–electron interactions modifies the orbital resolved (Figure 3) and total (Figure 4) density-of-states (DOS) within the Mo^{4+} $(4d^2)$ configuration of MoO_2. Likewise for VO_2 [5], MO dynamical correlations arising from U, U' and J_H lead to spectral weight redistribution over large energy scales and the formation of lower- (LHB) and upper-Hubbard (UHB) bands. Remarkable differences in the spectral weight transfer (SWT) is seen between the $x^2 - y^2$ and the yz, xz channels. In the upper panel of Figure 3 we show the LDA+DMFT DOS of the $x^2 - y^2$-orbital, whose evolution as function of U is crucial for understanding the role of intra- and inter-orbital dynamical correlations mutually assisting the orbital reconstruction and Mott-Peierls instability in MoO_2. As seen, the incipient LHB at $\omega \approx -2.4$ eV for $U = 2$ eV is transfered to higher binding energies, becoming more pronounced with increasing U. On the other hand, the UHB is not clearly resolved in the $x^2 - y^2$ orbital. Indeed, we observe a sharp antibonding-like peak at energies above 3.0 eV and a shoulder feature at $\omega \simeq 2.2$ eV, both being pushed higher in energy with increasing U. Correlation effects are, however, more visible at the bonding state. This quasi-localized band centered at -1.2 eV in LDA (solid line in Figure 1) is dynamically transferred to lower energies, spanning across E_F for 2.0 eV $\leq U \leq$ 3.0 eV. In contrast to cluster-DMFT results for VO_2 [5], where narrow bonding states are located below E_F, with $U \geq 4$ eV we find them above E_F, yielding a pseudogaped, metallic state in $x^2 - y^2$ electronic channel, as in Figure 3.

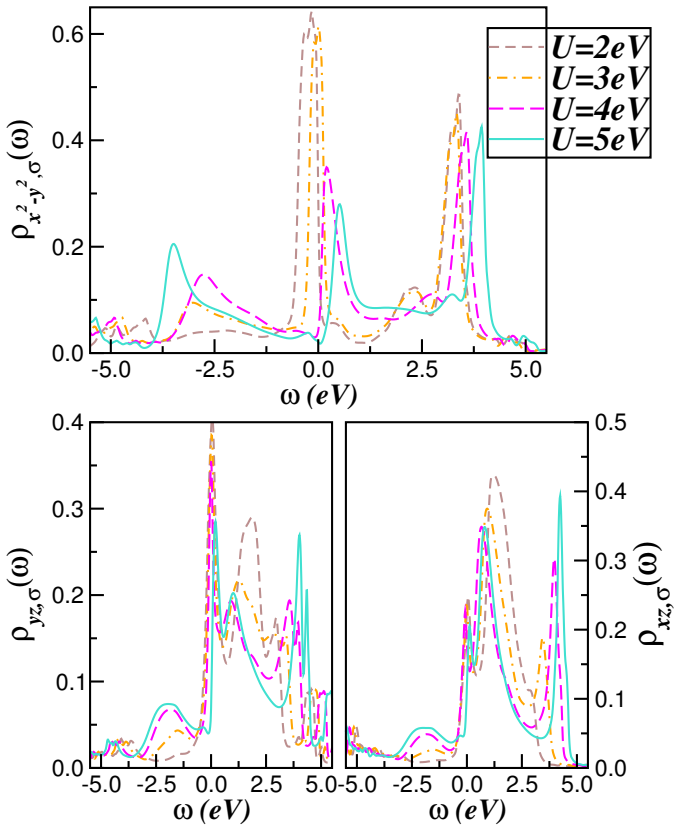

Figure 3. Effect of electronic correlations on the orbital-resolved LDA+DMFT density-of-states (DOS) of monoclinic MO_2. Worth noticing is the dynamical evolution of the $d_{x^2-y^2}$ bonding-antibonding branch, which shows an overall shift to energies above E_F due to correlation-induced spectral weight transfer. Also relevant is the formation of a pseudogap-like state at energies near the Fermi level ($E_F = \omega = 0.0$) for $U = 5$ eV.

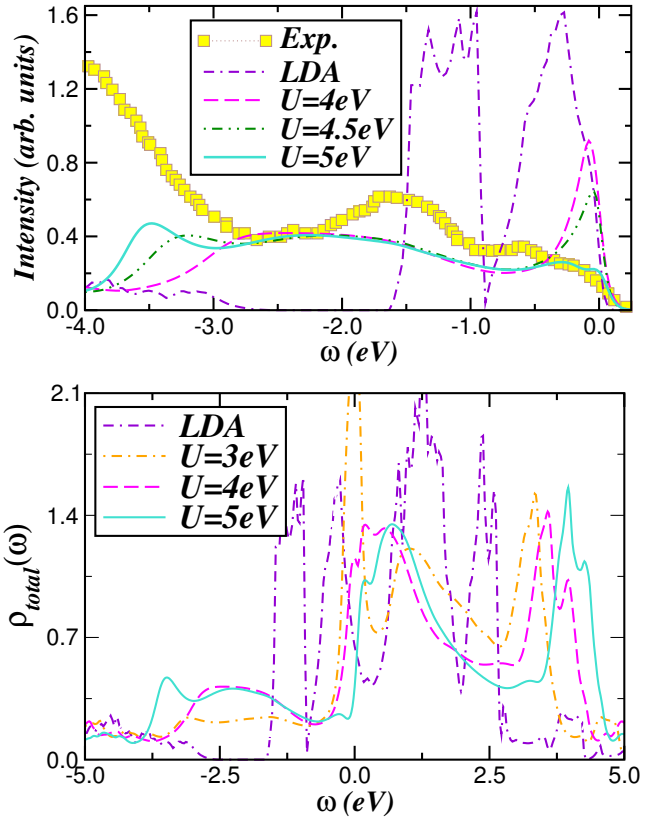

Figure 4. Bottom panel: Role of electron–electron interactions on the total LDA+DMFT DOS. LDA results are shown for comparison. Notice the formation of a lower Hubbard band at energies close to -2 eV and the evolution of the reconstructed electronic structure above E_F. The top panel shows the theory-experiment comparison between LDA+DMFT one-particle spectral functions and the photoemission spectra taken from Ref. [19]. Notice the good theory-experiment agreement at low energies and the correlation induced transfer of spectral weight compared to LDA from low to high binding energies.

Appreciable SWT within the yz, xz-orbitals is also visible in the lower panels of Figure 3. Interestingly, electronic interactions in these orbitals lead to sharp quasiparticle peaks close to E_F. These collective Kondo-like resonances move to energies close to 0.1 eV at $U = 5$ eV with concomitant appearance of pseudogaped electronic states in the xz, yz orbitals. Moreover, given sizable U', interband dynamical proximity effects between $x^2 - y^2$ and yz, xz orbitals yield the creation of bonding-antibonding bands in the yz, xz channels. Correlated electron features in the valence band DOS will lead to local magnetic moments associated with the developing of a prominent LHB in the $x^2 - y^2$ orbital. Noteworthy, magnetic ordering and unconventional superconductivity ($T_c = 7$ K) were observed in potassium-doped MoO_2 samples, $K_xMoO_{2-\delta}$ [37]. In these compounds, X-ray powder-diffraction data suggest that K-atoms increase the lattice parameters of the monoclinic structure with increasing K composition. Taken together these observations with our LDA+DMFT results suggest that under strain, inducing band narrowing due to expansion of the lattice crystal structure, anisotropic excitations would be seen in magnetic susceptibility data of pure MoO_2 at low T.

The bottom panel of Figure 4 displays the total LDA and LDA+DMFT spectral function. As a major effect of electron–electron interactions, the bonding-antibonding feature in LDA re-emerges and persists above E_F with increasing U for all three orbitals. From this result we can now draw the following conclusion: The bonding-antibonding states (reflecting charge localization within Mo-Mo dimers in LDA, see Figure 1) are transferred to energies above E_F by MO dynamical correlations.

Interestingly, our LDA+DMFT band splitting is consistent with soft-X-ray absorption spectra [20], showing two main broad features separated by almost 4 eV as in Figure 4. Extant PES and ARPES data can also be interpreted on the basis of our correlated electronic structure. An ARPES study [19] shows a broad maximum around 0.2 eV binding energy which moves towards to E_F with increasing the emission angle and the photon energy. We assign this primary maximum as the small bump found for $U = 5$ eV at $\omega = -0.28$ eV, as shown in the top panel of Figure 4. Smaller U values provide a huge peak at low binding energies which is not seen in experiment [19]. Importantly, the LDA+DMFT results for $U = 5$ eV show good agreement with PES data [19] at low energies, implying the suppression of the Landau-FL coherence in the electronic states and unconventional metallicity in pure and doped MoO_2 systems [37]. Moreover, valence band spectra recorded on thin films show an energy band peaked at -1.8 eV, consistent with our LHB centered at energies close to -2.2 eV. It is worth noting that this value coincides with the energy gap in LDA where oxygen p-bands start. The fact that this bare band gap is not seen in PES experiments [20] is the one-particle fingerprint of dynamical MO correlations, and goes beyond previous ab initio formulations for monoclinic MoO_2.

Understanding the modification of anisotropic charge dynamics in MoO_2 promises to shed light upon the precise nature of the reconstructed (by dynamical correlations) orbital state discussed above. Our LDA+DMFT results in Figure 3 show how MO electronic correlations self-organize the one-particle spectral functions of monoclinic MoO_2. While the xz-orbital DOS unveil maximum itinerancy at large U (see our results below) and has a shape similar to yz-orbital, the more localized $x^2 - y^2$ orbital-DOS shows completely different lineshape. SWT over large energy scales O (8.0 eV) is also apparent in Figures 3 and 4. In our MO-DMFT calculation, inter-orbital charge transfer leads to spectral weight redistribution between the different d-orbital DOS. This is a characteristic also exhibited by other correlated MO systems [38], and points to the relevance of MO correlations in the electronic structure of MoO_2.

2.2. Optical Conductivity

We now present the optical conductivity and galvanostatic, voltage-capacity profiles of MoO_2 battery material using the LDA+DMFT propagators for the most relevant $4d$-orbitals discussed above. In the limit of high lattice dimensions, the optical response is directly evaluated as convolution of the DMFT propagators [8]. For MO systems, the real part of the optical conductivity can be written as $\sigma'_{a,\sigma}(\omega) = \gamma_a \sum_{\mathbf{k}} \int d\omega' \frac{f(\omega')-f(\omega+\omega')}{\omega} A_{\mathbf{k},a,\sigma}(\omega'+\omega) A_{\mathbf{k},a,\sigma}(\omega')$, where $\gamma_a \equiv v_a^2 \frac{2\pi e^2 \hbar}{V}$ and V is the volume of the unit cell per formula unit, v_a is the fermion velocity in orbital a, $A_{a,\sigma}(\mathbf{k},\omega)$ is the corresponding fully renormalized one-particle spectral function and $f(\omega)$ is the Fermi distribution function. Within our correlated, MO scheme the complex optical conductivity is given by $\sigma(\omega) = \sum_{a,\sigma}[\sigma'_{a,\sigma}(\omega) + i\sigma''_{a,\sigma}(\omega)]$. Hence, using the Kramers–Krönig relations [39,40], the complex dielectric function $\varepsilon(\omega) = 1 + \frac{4\pi i \sigma(\omega)}{\omega}$ can be computed for the metallic state relevant to MoO_2, providing a microscopic scheme to study the voltage-capacity profiles of correlated battery materials [41]. However, as in our earlier study of normal-state electrodynamic responses of LaOFeAs the approximation made here is to ignore the $\mathbf{k}$-dependence of electron's velocity, $v_{\mathbf{k},a}$. In this situation, following Saso et al. [42], we approximate $v_{\mathbf{k},a}$ by a single average carrier velocity ($v_a = v$) for all orbitals. This assumption works well for numerical computations of optical conductivity responses of Kondo insulators (FeSi and YbB_{12}) [42], V_2O_3 [43], $3d^1$ perovskite titanates [44], and to lithium-ion battery materials [41], supporting our approximation in $\sigma'_{a,\sigma}(\omega)$ above. The observed features in optical conductivity originate from correlation induced spectral changes: Showing how this provides a compelling description of extant experimental data [22] is our focus here.

In Figure 5 we show the real part of the orbital-resolved optical conductivity computed within the LDA+DMFT scheme. As expected, our formulation reveals a Drude-like peak in the coherent FL regime at $U \leq 3$ eV. Moreover, as found in other correlated metals, large-scale two-particle SWT with increasing U is also explicit in our results. In MoO_2 this is linked to the reconstructed orbital bonding-antibonding state in the correlated MO problem. An additional interesting feature in our

results is the damped Drude component at $U = 5$ eV in the yz orbital. This behavior is characteristic of a bad metal, and it is consistent with the emergent pseudogaped spectral function as shown in Figure 3. However, the most interesting aspect of our many-particle description are the non-FL features within the $x^2 - y^2$ orbital at $U \geq 4$ eV. At $U = 4$ eV we observe two peaks at 0.2 eV and 3.0 eV, which can be understood as particle-hole excitations (of the two-particle Green's function related to the current-current correlation function in DMFT) from the valence band to the reconstructed bonding-antibonding bands above E_F, see Figure 3. As expected, with increasing U these two optical peaks are shifted to higher energies, and for $U = 4.5$ eV we observe them at 0.72 eV and 3.37 eV. Similar features as shown for $U = 4.5$ eV, i.e., very narrow Drude low-energy part followed by two peaks were resolved in the optical spectra of MoO_2 [22]. According to our results, the first peak at 0.8 eV in optics [22] is interpreted as electronic excitations within the $x^2 - y^2$ orbital from the LHB to a fully renormalized conduction band. The agreement between theory and experimental data could be further improved by tuning the on-site Coulomb interaction strength in the $x^2 - y^2$ orbital sector of MoO_2. On the other hand, the method presented here is clearly performing robustly even for a first guess of U, which makes our approach suitable for a rapid scan and characterisation of battery materials candidates. Taken theory and experiment together, our work microscopically reconciles the most salient low-energy features seen in optical (Figure 5) and PES (Figure 4) experiments, showing the relevance of sizable electronic correlations (1.0 eV $\leq U/W \leq$ 1.1 eV, here $W \approx 4.5$ eV is the one-electron LDA bandwidth) in MoO_2.

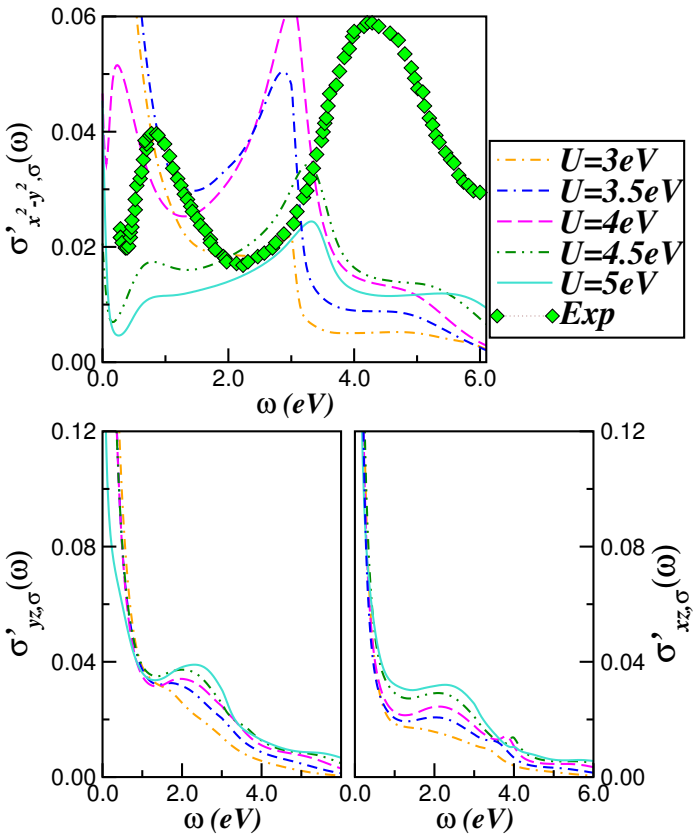

Figure 5. Orbital resolved optical conductivity of monoclinic MoO_2 computed within LDA+DMFT. Notice the changes in the Drude-like peak below 0.5 eV and its evolution with increasing U. For the $x^2 - y^2$ orbital also relevant is the energy position of the first optical conductivity peak at 0.72 eV for $U = 4.5$ eV which is in semi-qualitative agreement with experimental data taken from Ref. [22]. As discussed in the text, the two main peaks in optics are fingerprints of particle-hole excitations within the correlated monoclinic phase of MoO_2.

2.3. Voltage-Capacity Using LDA+DMFT

Optical spectroscopy experiments are important for characterizing charge dynamics in solids [40]. Specifically, they measure how particle-hole excitations propagates in the system, uncovering the detailed nature of the excitation spectrum itself. Motivated by our earlier studies on two-particle responses of lithium-ion battery materials [41] in this work we show that coherent and incoherent propagation of particle-hole pair excitations built from correlated electronic states are also applicable to understanding charge/discharge experiments of anodic MoO_2 battery material [16,27]. To benchmark a microscopic description of quantum capacity, we recall that capacitance of a flat circular disk of radius R is given by $C = 8R\varepsilon$ [45], with ε being the dielectric constant. To make progress, we assume (i) that linear relation with a constant slope holds true for moderate values of voltage V, i.e., $C(V) \approx \varepsilon(V)$, as well as (ii) that the energy of electron-hole pair excitation probed in optical spectroscopy is close to the potential change of the battery material during charge/discharge, i.e., $\omega \cong V$. With these assumptions we have established [41] an analogy between electrodynamics and charging experiments as long as $C(V) \cong |\varepsilon(\omega)|$. Thus, one can use our results for the complex dielectric function $\varepsilon(\omega) = 1 + \frac{4\pi i\sigma(\omega)}{\omega}$ (not shown) to clarify intrisic features seen in the voltage profile of charge/discharge rate capabilities [16,27].

Let us now discuss the implications of our results for a microscopic understanding of voltage-capacity profiles of MoO_2 battery material. We shall first recall that in experiments the charge-discharge cycling is limited to the potential window between 0.5 to 2.5 V [16,27]. However, the two main charge plateaus in galvanostatic charge and discharge curves seen in experiments are mostly located at voltage range between 1.3 and 1.8 V [15,16,27]. Hence, as displayed in Figure 6, the MoO_2 electrodes have two potential plateaus at about 1.5 V and 1.3 V for lithium insertion [16,27], and the voltage drop between these two plateaus is usually ascribed to a phase transition from monoclinic to a orthorhombic lattice structure upon Li insertion [27]. Moreover, it is also noteworthy that MoO_2 nanoplates [46] and nanorods [47] have excellent electrochemical and cycling performance when the discharge cutoff voltage is set close to 1.0 V [46]. With this caveats in mind, in Figure 6 we show our results for voltage versus capacity of discharged MoO_2 using our relation $C(V) \cong |\varepsilon(\omega)|$ for the quantum capacity of battery materials [41].

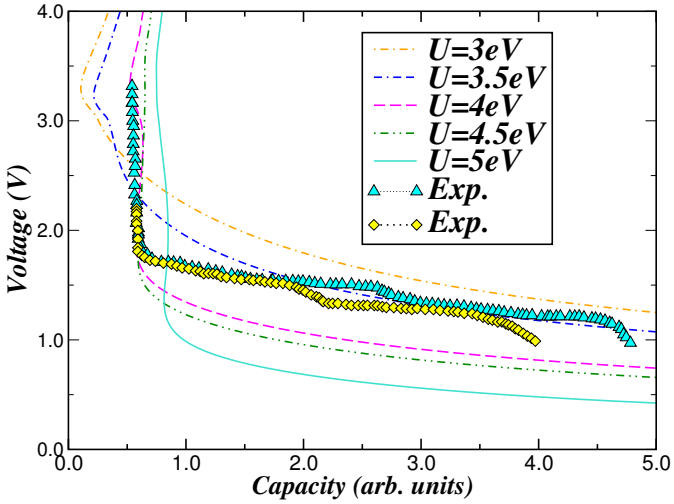

Figure 6. Rate capability of stoichiometric MoO_2 within LDA+DMFT in the potential (V) window relevant for future battery applications. Experimental voltage-capacity profiles of MoO_2 taken from Refs. [27] (triangles) and [16] (diamond) are shown for comparison. (The experimental data was shifted upward to coincide with theory at low specific capacities.) Notice the good qualitative agreement between the experimental data and the LDA+DMFT results for $U = 3.5$ eV.

As seen in Figure 6, stoichiometric MoO_2 has large potential versus capacity traces at two characteristic values between 1.5 to 0.9 V for 3.0 eV$\leq U \leq$ 4.0 eV; and good qualitative agreement with experiments at finite capacity values is obtained using the LDA+DMFT results for $U = 3.5$ eV. Our description in Figure 6 thus implies that characteristic voltage-capacity profiles of MoO_2 anode material [16,27] are originated from intrinsic optical spectral weight transfer in $\sigma(\omega)$ (from where the quantum capacity $C(V)$ is computed) [41] due to particle-hole excitations within the $x^2 - y^2, yz, xz$ channels of MoO_2. Interestingly, the V-dependence of our LDA+DMFT results for $4.0 \leq U \leq 4.5$ eV are also consistent with experimental results in the low capacity range where the voltage increases abruptly. This in turn suggests that the nearly undoped compound is in a sizable correlated regime and that electronic correlations are slightly reduced upon lithiation, driving the anode material to a regime where the on-site Coulomb repulsion is close to 3.5 eV. Thus, according to our theory-experiment comparison, for capacity values above 1.8 where good agreement is seen in Figure 6 correlation effects are predicted to be partially screened in Li-doped MoO_2 and this might be the electronic mechanism for the monoclinic-to-orthorhombic structural transition observed during lithiation insertion reaction [27]. In this scenario, the volume change caused by the monoclinic-to-orthorhombic structural transition observed during lithium insertion reaction correlates with partial screening of correlation effects in electron-doped MoO_2, which lowers on-site Coulomb repulsions. If this electronic factor alone can be taken as driving force for the structural distortion, then strained MoO_2 may offer a means to minder volume changes by keeping the material in a regime of stronger correlation effects, where strain can contrast the screening effect of electron-doping by Li insertion.

Together with our previous work on Li_2MoO_3 cathode material [48], the results presented here prove the applicability and transferability of this approach to battery materials in general, anodic and cathodic, towards a precise and computationally efficient characterisation of voltage-capacity profiles in battery cells and devices. At the same time, this approach allows distinguishing between cathode and anode battery materials candidates, within a database search or a crystal structure prediction workflow. We expect this work to prompt further application of this computational strategy for novel battery products.

3. Materials and Methods

The local-density-approximation plus dynamical-mean-field-theory (LDA+DMFT) is used, which by construction includes the most relevant multi-orbital correlation effects and all-electron degrees of freedom. The LDA+DMFT scheme is ideally suited for the investigation of Coulomb-driven metal-to-insulator transitions, Fermi and non-Fermi liquid metallic states, as it best captures dynamical correlations in idealized many-particle models as well as in real multi-orbital systems [8]. The LDA+DMFT method is a theoretical framework and a numerical tool, which provides insights into fundamental questions like for example the existence of orbital and magnetic orders in strongly correlated electron systems at low temperatures, as well as their response upon application of external perturbations. The one-particle, LDA density-of-states are computed using the non-fully relativistic version of the PY-LMTO code [30]. To incorporate the effects of dynamical electronic correlations in this 4*d* transition-metal oxide, the multi-orbital iterated-perturbation-theory (MO-IPT) was used as an impurity solver of the many-particle problem in DMFT, as described in detail in Refs. [31].

4. Conclusions

In summary, a comprehensive study of orbital-selective electronic reconstruction, optical and galvanostatic responses in MoO_2 is presented in this work. In general, the good qualitative agreement between our theoretical results and those observed in photoemission and optical conductivity measurements support our view of sizable dynamical correlations as the driving mechanism towards an orbital bonding-antibonding state reconstruction in monoclinic transition-metal dioxides. Existence of Mo-Mo dimers along the *c*-axis follows as a consequence of multi-orbital proximity effect in the orbital-selective metallic regime of MoO_2. Our description of an electronic orbital reconstructed state

has broad applications for the detailed investigation of doped molybdenum dioxide systems showing unconventional metallic behavior at low temperatures [23,37]. It is also expected to open a new pathway in understanding the physical properties of Mo-based [49,50] and other families of correlated battery materials [48,51–53] with large Li-storage capacity and enhanced reversibility efficiency.

Author Contributions: S.L. carried out the LDA (LMTO-based) calculations. L.C. designed and carried out the LDA+DMFT study. All authors contributed to the scientific discussion, data analysis, interpretation, data visualisation and to the preparation of the manuscript, and approved the final version of the manuscript. All authors have read and agreed to the published version of the manuscript.

Funding: L.C.'s work is supported by CNPq (Grant No. 304035/2017-3).

Acknowledgments: Acknowledgment (L.C.) is made to CAPES. S.L. thanks ARCCA Cardiff for computational resources. Via S.L.'s membership of the UK's HPC Materials Chemistry Consortium, which is funded by EPSRC (No. EP/L000202), this work made use of the facilities of ARCHER, the UK's National High-Performance Computing Service, which is funded by the Office of Science and Technology through EPSRC's High End Computing Programme.

Conflicts of Interest: The authors declare no conflict of interest.

References

1. Imada, M.; Fujimori, A.; Tokura, Y. Metal-insulator transitions. *Rev. Mod. Phys.* **1998**, *70*, 1039–1263. [CrossRef]
2. Juliano, R.C.; de Arruda, A.S.; Craco, L. Coexistence and competition of on-site and intersite Coulomb interactions in Mott-molecular-dimers. *Solid State Commun.* **2016**, *227*, 51–55. [CrossRef]
3. Peierls, R.E. *Quantum Theory of Solids*; Oxford University Press: Oxford, UK, 1955.
4. Qazilbash, M.M.; Brehm, M.; Chae, B.-G.; Ho, P.-C.; Andreev, G.O.; Kim, B.-J.; Yun, S.J.; Balatsky, A.V.; Maple, M.B.; Keilmann, F.; et al. Mott transition in VO_2 revealed by infrared spectroscopy and nano-imaging. *Science* **2007**, *318*, 1750–1753. [CrossRef] [PubMed]
5. Biermann, S.; Poteryaev, A.; Lichtenstein, A.I.; Georges, A. Dynamical singlets and correlation-assisted peierls transition in VO_2. *Phys. Rev. Lett.* **2005**, *94*, 026404. [CrossRef] [PubMed]
6. Brito, W.H.; Aguiar, M.G.O.; Haule, K.; Kotliar, G. Metal-insulator transition in VO_2: A DFT+DMFT perspective. *Phys. Rev. Lett.* **2016**, *117*, 056402. [CrossRef]
7. Chakhalian, J.; Freeland, J.W.; Habermeier, H.-U.; Cristiani, G.; Khaliullin, G.; van Veenendaal, M.; Keimer, B. Orbital reconstruction and covalent bonding at an oxide interface. *Science* **2007**, *318*, 1114–1117. [CrossRef]
8. Kotliar, G.; Savrasov, S.Y.; Haule, K.; Oudovenko, V.S.; Parcollet, O.; Marianetti, C.A. Electronic structure calculations with dynamical mean-field theory. *Rev. Mod. Phys.* **2006**, *78*, 865–951. [CrossRef]
9. Ma, C.-H.; Lin, J.-C.; Liu, H.-J.; Do, T.H.; Zhu, Y.-M.; Ha, T.D.; Zhan, Q.; Juang, J.-Y.; He, Q.; Arenholz, E.; et al. Van der Waals epitaxy of functional MoO_2 film on mica for flexible electronics. *Appl. Phys. Lett.* **2016**, *108*, 253104. [CrossRef]
10. Kwon, B.W.; Ellefson, C.; Breit, J.; Kim, J.; Norton, M.G.; Ha, S. Molybdenum dioxide-based anode for solid oxide fuel cell applications. *J. Power Sources* **2013**, *243*, 203–210. [CrossRef]
11. Bhosle, V.; Tiwari, A.; Narayan, J. Epitaxial growth and properties of $MoO_x(2 < x < 2.75)$ films. *J. Appl. Phys.* **2005**, *97*, 083539.
12. Shon, J.K.; Lee, H.S.; Park, G.O.; Yoon, J.; Park, E.; Park, G.S.; Kong, S.S.; Jin, M.; Choi, J.-M.; Chang, H.; et al. Discovery of abnormal lithium-storage sites in molybdenum dioxide electrodes. *Nat. Comm.* **2016**, *7*, 11049. [CrossRef]
13. Shi, Y.; Guo, B.; Corr, S.A.; Shi, Q.; Hu, Y.-S.; Heier, K.R.; Chen, L.; Seshadri, R.; Stucky, G.D. Ordered mesoporous metallic MoO_2 materials with highly reversible lithium storage capacity. *Nano Lett.* **2009**, *9*, 4215–4220. [CrossRef] [PubMed]
14. Yang, L.C.; Gao, Q.S.; Tang, Y.; Wu, Y.P.; Holze, R. MoO_2 synthesized by reduction of MoO_3 with ethanol vapor as an anode material with good rate capability for the lithium ion battery. *J. Power Sources* **2008**, *179*, 357–360. [CrossRef]
15. Sun, Y.; Hu, X.; Yu, J.C.; Li, Q.; Luo, W.; Yuan, L.; Zhang, W.; Huang, Y. Morphosynthesis of a hierarchical MoO_2 nanoarchitecture as a binder-free anode for lithium-ion batteries. *Energy Environ. Sci.* **2011**, *4*, 2870-2877. [CrossRef]

16. Sen, U.K.; Shaligram, A.; Mitra, S. Intercalation anode material for lithium ion battery based on molybdenum dioxide. *ACS Appl. Mater. Interfaces* **2014**, *6*, 14311–14319. [PubMed]
17. Katayama, N.; Takeda, H.; Yamaguchi, T.; Yamada, Y.; Iida, K.; Takigawa, M.; Ohta, Y.; Sawa H. Robust atomic orbital in the cluster magnet $LiMoO_2$. *Phys. Rev. B* **2020**, *102*, 081106. [CrossRef]
18. Alves, L.M.S.; dos Santos, C.A.M.; Benaion, S.S.; Machado, A.J.S.; de Lima, B.S.; Neumeier, J.J.; Marques, M.D.R.; Aguiar, J.A.; Mossanek, R.J.O.; Abbate, M. Superconductivity and magnetism in the $K_xMoO2_{2-\delta}$. *J. Appl. Phys.* **2012**, *112*, 073923. [CrossRef]
19. Moosburger-Will, J.; Kündel, J.; Klemm, M.; Horn, S.; Hofmann, P.; Schwingenschlögl, U.; Eyert, V. Fermi surface of MoO_2 studied by angle-resolved photoemission spectroscopy, de Haas–van Alphen measurements, and electronic structure calculations. *Phys. Rev. B* **2009**, *79*, 115113. [CrossRef]
20. Eyert, V.; Horny, R.; Höck, K.-H.; Horn, S. Embedded Peierls instability and the electronic structure of MoO_2. *J. Phys. Condens. Matter* **2000**, *12*, 4923–4946. [CrossRef]
21. Davenport, M.A.; Krogstad, M.J.; Whitt, L.M.; Hu, C.; Douglas, T.C.; Ni, N.; Rosenkranz, S.; Osborn, R.; Allred, J.M. Fragile 3D Order in $V_{1-x}Mo_xO_2$. *arXiv* **2019**, arXiv:1909.12704.
22. Chase, L.L. Optical properties of CrO_2 and MoO_2 from 0.1 to 6 eV. *Phys. Rev. B* **1974**, *10*, 2226–2231. [CrossRef]
23. Prakash, R.; Phase, D.M.; Choudhary, R.J.; Kumar, R. Structural, electrical, and magnetic properties of $Mo_{1-x}Fe_xO_2$ (x = 0–0.05) thin films grown by pulsed laser ablation. *J. Appl. Phys.* **2008**, *103*, 043712 . [CrossRef]
24. Scanlon, D.O.; Watson, G.W.; Payne, D.J.; Atkinson, G.R.; Egdell, R.G.; Law, D.S.L. Theoretical and experimental study of the electronic structures of MoO_3 and MoO_2. *J. Phys. Chem. C* **2010**, *114*, 4636–4645. [CrossRef]
25. Ataca, C.; Şahin, H.; Ciraci, S. Stable, Single-layer MX_2 transition-metal oxides and dichalcogenides in a honeycomb-like structure. *J. Phys. Chem. C* **2012**, *116*, 8983–8999. [CrossRef]
26. Wadati, H.; Yoshimatsu, K.; Kumigashira, H.; Oshima, M.; Sugiyama, T.; Ikenaga, E.; Fujimori, A.; Mravlje, J.; Georges, A.; Radetinac, A.; et al. Photoemission and DMFT study of electronic correlations in $SrMoO_3$: Effects of Hund's rule coupling and possible plasmonic sideband. *Phys. Rev. B* **2014**, *90*, 205131. [CrossRef]
27. Kim, A.; Park, E.; Lee, H.; Kim, H. Highly reversible insertion of lithium into MoO_2 as an anode material for lithium ion battery. *J. Alloys Compd.* **2016**, *681*, 301–306. [CrossRef]
28. Craco, L.; Leoni, S. Mott and pseudogap localization in pressurized NbO_2. *Phys. Rev. B* **2020**, in press. [CrossRef]
29. Brito, W.H.; Aguiar, M.C.O.; Haule, K.; Kotliar. Dynamic electronic correlation effects in NbO_2 as compared to VO_2. *Phys. Rev. B* **2017**, *96*, 195102. [CrossRef]
30. Chadov, S.; Qi, X.; Kübler, J.; Fecher, G.H.; Felser, C.; Zhang, S.C. tunable multifunctional topological insulators in ternary Heusler compounds. *Nat. Mater.* **2010**, *9*, 541–545. [CrossRef]
31. Craco, L. Quantum orbital entanglement: A view from the extended periodic Anderson model. *Phys. Rev. B* **2008**, *77*, 125122. [CrossRef]
32. Laad, M. S.; Craco, L.; Müller-Hartmann, E., Orbital-selective insulator-metal transition in V_2O_3 under external pressure. *Phys. Rev. B* **2006**, *73*, 045109. [CrossRef]
33. Grenzebach, C.; Anders, F.B.; Czycholl, G.; Pruschke, T. Transport properties of heavy-fermion systems.*Phys. Rev. B* **2006**, *74*, 195119. [CrossRef]
34. Tomczak, J.M.; Biermann, S. Optical properties of correlated materials: Generalized Peierls approach and its application to VO_2. *Phys. Rev. B* **2009**, *80*, 085117. [CrossRef]
35. Laad, M.S.; Craco, L.; Leoni, S.; Rosner, H. Electrodynamic response of incoherent metals: Normal phase of iron pnictides. *Phys. Rev. B* **2009**, *79*, 024515. [CrossRef]
36. Brandt, B.G.; Skapski, A.C. Refinement of the crystal structure of molybdenum dioxide. *Acta Chem. Scand.* **1967**, *21*, 661–672. [CrossRef]
37. Alves, L.M.S.; Damasceno, V.I.; dos Santos, C.A.M.; Bortolozo, A.D.; Suzuki, P.A.; Izario Filho, H.J.; Machado, A.J.S.; Fisk, Z. Unconventional metallic behavior and superconductivity in the K-Mo-O system. *Phys. Rev. B* **2010**, *81*, 174532. [CrossRef]
38. Lechermann, F.; Biermann, S.; Georges, A. Competing itinerant and localized states in strongly correlated $BaVS_3$. *Phys. Rev. B* **2007**, *76*, 085101. [CrossRef]

39. Bobrov, V. B.; Trigger; S. A.; van Heijst., G. J. F.; Schram, P. P. J. M. Kramers-Kronig relations for the dielectric function and the static conductivity of Coulomb systems. *Europhys. Lett.* **2010**, *90*, 10003. [CrossRef]
40. Basov, D.N.; Averitt, R.D.; van der Marel, D.; Dressel, M.; Haule, K. Electrodynamics of correlated electron materials. *Rev. Mod. Phys.* **2011**, *83*, 471–541. [CrossRef]
41. Craco, L.; Leoni, S. Electrodynamics and quantum capacity of Li_xFePO_4 battery material. *Appl. Phys. Lett.* **2011**, *99*, 192103. [CrossRef]
42. Urasaki, K.; Saso, T. correlation effects on optical conductivity of FeSi. *J. Phys. Soc. Jpn.* **1999**, *68*, 3477–3480. [CrossRef]
43. Baldassarre, L.; Perucchi, A.; Nicoletti, D.; Toschi, A.; Sangiovanni, G.; Held, K.; Capone, M.; Ortolani, M.; Malavasi, L.; Marsi, M.; et al. Quasiparticle evolution and pseudogap formation in V_2O_3: An infrared spectroscopy study. *Phys. Rev. B* **2008**, *77*, 113107. [CrossRef]
44. Pavarini, E.; Yamasaki, A.; Nuss, J.; Andersen, O.K. How chemistry controls electron localization in $3d^1$ perovskites: A Wannier-function study. *New J. Phys.* **2005**, *7*, 188. [CrossRef]
45. Ferry, D.; Goodnick, S.M. *Transport in Nanostructures*; Cambridge University Press: Cambridge, UK, 1997.
46. Liu, X.; Yang, J.; Hou, W.; Wang, J.; Nuli, Y. Highly reversible lithium-ions storage of molybdenum dioxide nanoplates for high power lithium-ion batteries. *Chem. Sustain. Chem.* **2015**, *8*, 2621–2624. [CrossRef]
47. Guo, B.; Fang, X.; Li, B.; Shi, Y.; Ouyang, C.; Hu, Y.-S.; Wang, Z.; Stucky, G.D.; Cheng, L. Synthesis and lithium storage mechanism of ultrafine MoO_2 nanorods. *Chem. Mater.* **2012**, *24*, 457–463. [CrossRef]
48. Baldoni, M.; Craco, L.; Seifert, G.; Leoni, S. A two-electron mechanism of lithium insertion into layered α-MoO_3: A DFT and DFT+U study. *J. Mat. Chem. A* **2013**, *1*, 1778–1784. [CrossRef]
49. Wang, W.; Qin, J.; Yin, Z.; Cao, M. Achieving fully reversible conversion in MoO_3 for lithium ion batteries by rational introduction of $CoMoO_4$. *ACS Nano* **2016**, *10*, 10106–10116. [CrossRef]
50. Gao, S.; Tang, Y.; Gao, Y.; Liu, L.; Zhao, H.; Li, X.; Wang, X. Highly Crystalized $Co_2Mo_3O_8$ hexagonal nanoplates interconnectedby coal-derived carbon via the molten-salt-assisted method forcompetitive li-ion battery anodes. *ACS Appl. Mater. Interfaces* **2019**, *11*, 7006–7013. [CrossRef]
51. Cabana, J.; Monconduit, L.; Larcher, S.; Palacín, M.R. Beyond Intercalation-Based Li-ion Batteries: The State of the Art and Challenges of Electrode Materials Reacting Through Conversion Reactions. *Adv. Energy Mater.* **2010**, *22*, E170–E192. [CrossRef]
52. Zhou, Y.-N.; Ma, J.; Hu, E.; Yu, X.; Gu, L.; Nam, K.-W.; Chen, L.; Wang, Z.; Yang, X.-Q. Tuning charge-discharge induced unit cell breathing in layer-structured cathode materials for lithium-ion batteries. *Nat. Comm.* **2014**, *5*, 538. [CrossRef]
53. Meng, T.; Hao, Y.-N.; Qin, J.; Cao, M. Interface-engineering-induced electric field effect and atomic disorder in cobalt selenide for high-rate and large-capacity lithium storage. *ACS Sustain. Chem. Eng.* **2019**, *7*, 4657–4665. [CrossRef]